Available online at www.sciencedirect.com
SCIENCE DIRECT
Journal of Magnetic Resonance 180 (2006) 286–296
JMR Journal of Magnetic Resonance
www.elsevier.com/locate/jmr

Dynamic shim updating on the human brain

Kevin M. Koch *, Scott McIntyre, Terence W. Nixon, Douglas L. Rothman, Robin A. de Graaf

Magnetic Resonance Research Center, Yale University, New Haven, CT, USA

Received 1 February 2006; revised 9 March 2006
Available online 30 March 2006

Abstract

Dynamic alteration of shim settings during a multi-slice imaging experiment can improve static magnetic-field homogeneity over extended volumes. In this report, a pre-emphasized dynamic shim updating (DSU) system capable of rapidly updating all non-degenerate zeroth through second-order shims is presented and applied to high-field multi-slice imaging studies on the human brain. DSU is utilized in both non-oblique and oblique slicing geometries while updating in-plane and through-slice shims. Image-based magnetic-field maps are used to quantify homogeneity improvements and comparisons are made on a slice-specific basis between static global shimming and increasing orders of shim inclusion utilized DSU. The influence of oblique slicing geometry on DSU-utilized global homogeneity is also quantified computationally. Finally, the effect of DSU on susceptibility artifact reduction in single-shot axial-sliced EPI is analyzed using experimental acquisitions.

Keywords: Homogeneity; Shimming; Dynamic shimming; Shim degeneracy

1. Introduction

Discontinuities in material magnetic susceptibility (χ_M) generate induction fields which perturb the static field utilized in magnetic resonance studies [1]. Air-tissue boundaries produce the most dominant perturbations inside biological samples, while bone-tissue and grey-white matter-CSF boundaries also slightly contribute to local in vivo inhomogeneity. Within the imaging community, such static-field inhomogeneity results in geometric distortion and through-slice signal reduction. Rapid gradient-echo imaging strategies are particularly vulnerable to these effects due to extended and unfocused T_2^* influenced phase evolution during k-space sampling. Spectroscopic images are also impacted significantly by losses in spectral resolution due to static-field inhomogeneity.

Field compensation through room temperature spherical harmonic shim coils is the primary mechanism used to mitigate these effects. Typical high-field human systems possess up to second or third-order shims. Though sophisticated methods have been developed to strengthen and purify these shims [2], global inhomogeneity across the entire human brain cannot accurately be compensated through their utilization. Within the human brain, perturbations near the auditory and sinus cavities, as well as those at the base of the brain (e.g., hippocampus), are the most problematic. These regions cannot be compensated using low-order static spherical harmonic shim optimization without compromising homogeneity in other regions of the brain.

Unique approaches to the global shimming problem include ferroshimming [3], local passive shimming [4], and local electro-shimming [5]. The problem can also be mediated using spherical harmonic shims when modeling inhomogeneity in a local fashion, thus providing low-order shims with increased selectivity when targeting highly inhomogeneous areas. Dynamic shim updating (DSU) [6–8] allows for such optimal local modeling and updating of shim values for separate volumes within a multi-volume acquisition protocol. It provides the means and ability to

* Corresponding author. Fax: +1 203 785 6643.
E-mail address: kevin.koch@yale.edu (K.M. Koch).

1090-7807/$ - see front matter © 2006 Elsevier Inc. All rights reserved.
doi:10.1016/j.jmr.2006.03.007

model and remove locally manageable inhomogeneity in a global fashion.

Previous DSU reports have outlined the hardware requirements necessary for updating of shim amplifiers and further demonstrated the primary utility of the principle. The current work makes the following novel extensions and investigations in the implementation of DSU.

First, DSU is applied using all zeroth through second-order shims on a 4 T human system, whereas previous DSU investigations have been applied on the human brain at 1.5 [8] and 2.1 T [6] using only first-order shims. Furthermore, all zeroth through second-order shim changes are pre-emphasized to allow rapid updating of all shims, thus making DSU compatible with the stringent timing required for fMRI and DTI studies. The detailed methods and limitations of shim-change pre-emphasis are also discussed.

Second, an analytic shim-degeneracy removal method is presented to allow for implementation of DSU in arbitrary oblique geometries. Demonstration of oblique-sliced DSU is of interest for applications such as targeted functional magnetic resonance imaging (fMRI) and general longitudinal imaging studies where identical anatomical structures must be sampled during subsequent scans. Degeneracy analysis is accomplished through projection of three-dimensional shim functions into two-dimensional imaging planes and corresponding construction of non-degenerate shim sets for specified windows of oblique-sliced angulation. DSU is then experimentally demonstrated in single-oblique slicing geometries utilizing this degeneracy analysis.

Third, the impact of various parameters on DSU efficacy in the human brain is explored in detail for the first time. Quantified slice-specific improvements are presented when comparing an optimal static global shim setting to DSU using first, second, and third-order shims. Global, and first through second-order DSU is quantified using experimentally measured field maps. The effect of third-order shims is simulated computationally using the measured field maps. Quantified global homogeneity is compared for all slicing geometries in the axial-coronal plane with increasing shim-inclusions. Homogeneity quantification is computationally simulated using analytic slice rotations of measured axial-field maps and oblique shim degeneracy analysis.

Finally, the capabilities of the DSU system to reduce image distortion and signal loss in rapid EPI are presented using experimental acquisitions. Significant homogeneity improvements are demonstrated, particularly near the sinuses. Potential further improvements using more restricted slice optimization regions are also discussed.

2. Theory

When optimizing the homogeneity of thin slices, different three-dimensional spherical harmonic shims can have the same functional form when constrained to a two-dimensional plane. This degrades the linear independence of shim functions and generates a degeneracy condition. For example, within an infinitely thin slice obliqued at 45° in the $z - y$ plane, the Z and Y shims will have identical functional forms. Linear optimization strategies will become ill-conditioned and iterative non-linear optimization strategies will struggle to converge when optimizing over such linearly dependent (degenerate) shim sets. A pragmatic solution to this problem was presented as a single-oblique slice-shimming technique using linear projection optimization over a three-dimensional slab centered on each slice [9]. However, linear projection methods are not designed for arbitrary-shaped optimization regions. Therefore, to maintain generality in optimization geometry, such methods were not utilized in the DSU implementation.

A slab optimization could in principle be applied by field mapping over arbitrarily shaped slice-specific ROIs. A three-dimensional slab for single-slice optimization would then need to include slices on either side of the target optimization slice. This introduces another compromising factor in application to slice-specific DSU. One must keep in mind that the through-slice dimension is required to break shim degeneracy and that the degeneracies are continuous numerical instabilities in the optimization procedure. Therefore, a slab consisting of 3 slices (1 for the target slice +2 for the adjacent slices) will (a) not possess enough through-slice information to accurately homogenize in this dimension, and (b) will not sufficiently break the degeneracy. Furthermore, the use of more slices on either side of the target slice would compromise the local optimization advantages of DSU.

Alternatively, Kim et al. [10] frame the shim optimization problem as a linear system of shim-functionals over arbitrary-shaped optimization ROIs. Within this framework, two-dimensional shim degeneracies manifest themselves as ill-conditioned matrices in the linear inversion. To address the numerical instability of an ill-conditioned inversion problem, the authors implemented a sophisticated regularization method in conjunction with SVD inversion of the shim matrix.

As an alternative to both methods, we have used two-dimensional degeneracy analysis to determine non-degenerate shim sets for specified imaging planes. The neglected shims are the generators of the ill-conditioned matrices in the aforementioned regularized linear optimization method. Thus, either method of coping with the degeneracies could be used with similar results. Given the two choices, we have implemented the analytic degeneracy removal because of its visually intuitive approach to the problem.

2.1. In-plane shims

2.1.1. Non-oblique slices

In-plane shim degeneracies for infinitesimally thin, non-oblique slices are readily determined by visual inspection. For example, when slicing in the Z direction, the only non-degenerate in-plane shims are X, Y, Z^2, XY,

Table 1
Spherical harmonic shim functions and SO projection relations for $\theta = 45°$ and $(r, s, p) = (z, y, x)$ gradient orientations

Shim	Function	$\theta = 45°$ Single Oblique Projection
X	x	x
Y	y	z
Z	z	z
Z^2	$z^2 - (x^2 + y^2)/2$	$(z^2 - x^2)/2$
ZX	zx	zx
ZY	zy	z^2
$X^2 - Y^2$	$x^2 - y^2$	$x^2 - z^2$
XY	$2xy$	$2xz$
Z^3	$z^3 - 3z(x^2 + y^2)/2$	$(z^3 - 3zx^2)/2$
Z^2X	$z^2x - x(x^2 + y^2)/4$	$-(x^3 + 3xz^2)/4$
Z^2Y	$z^2y - y(x^2 + y^2)/4$	$(3z^3 - zx^2)/4$
$Z(X^2 - Y^2)$	$z(x^2 - y^2)$	$zx^2 - z^3$
ZXY	$2zxy$	$2z^2x$
X^3	$x^3 - 3xy^2$	$x^3 - 3xz^2$
Y^3	$3x^2y - y^3$	$3x^2z - z^3$

$X^2 - Y^2$, Z^2X, Z^2Y, X^3, and Y^3 (see Table 1 for Cartesian shim functions). The remaining shims within the full set are all linear combinations of these shims (e.g., XZ becomes a X shim and Z^3 becomes a Z^2 shim with B_0 offset).

2.1.2. Oblique slices

Any arbitrary oblique slicing strategy can mathematically be represented by rotations through two Euler angles. To maintain generality, we start with a reference frame (r, s, p), where r, s, and p signify the read, slice, and phase image-space coordinates. Here (r, s, p) can represent any of the six (x, y, z) gradient orientation combinations. Using the convention of Goldstein [11], rotating (r, s, p) by Euler angles θ and ϕ provides the rotated coordinate frame (r', s', p'),

$$r' = r\cos\theta + s\sin\theta, \tag{1}$$

$$s' = s\cos\theta\cos\phi - r\cos\phi\sin\theta + p\sin\phi, \tag{2}$$

$$p' = p\cos\phi - s\cos\theta\sin\phi + r\sin\theta\sin\phi. \tag{3}$$

Fig. 1 illustrates the geometric formalism used for a single-oblique ($\phi = 0$) slicing protocol. Here, θ is a rotation angle defined in the plane of the r and s coordinate axes. A double-oblique protocol will rotate the imaging plane about an axis orthogonal to the single-oblique plane by an angle ϕ. The direction of the double-oblique rotation is uniquely determined by the chosen convention of Euler rotation.

The equation of an arbitrarily oriented two-dimensional plane (i.e., infinitesimally thin slice) in the rotated coordinate system is given by

$$s' = c, \tag{4}$$

where c is a constant. For convenience, we set $c = 0$ (corresponding to a slice through the magnet isocenter) since shim determination using this degeneracy analysis is independent of constant offsets. However, this simplification ignores the generation of lower-order shims in off-center slices, which will be discussed at the end of this section.

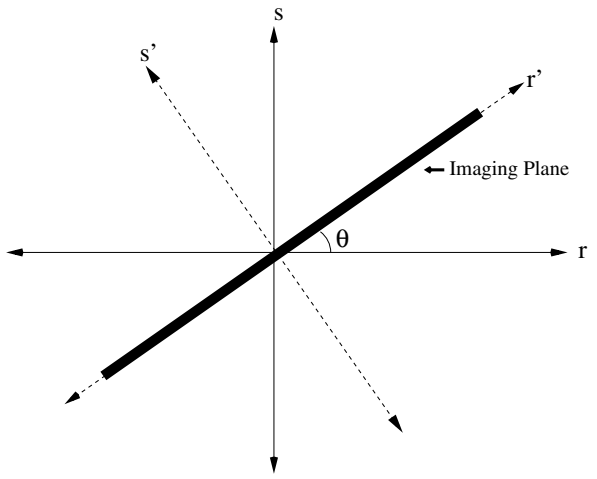

Fig. 1. Illustration of oblique-angulation coordinate formalism. A two-dimensional single-oblique ($\phi = 0$, $p = p'$) representation is depicted whereby the imaging plane is rotated in the r-s plane by an angle θ.

Inserting Eq. (4) into Eq. (2) gives the equation of an arbitrary oblique plane in the unrotated coordinates,

$$s\cos\theta\cos\phi - r\cos\phi\sin\theta + p\sin\phi = 0. \tag{5}$$

This relation can be used to remove a coordinate from the shim functions. The resulting expressions are then two-dimensional projections of the shims in the desired oblique plane centered on the origin. Analysis of these expressions allows for determination of proper non-degenerate sets of shims for use with any desired slicing geometry.

As an example, we consider a single-oblique (SO) rotation of $45° \rightarrow (\phi = 0°, \theta = 45°)$. In our current analysis this corresponds to slices obliqued in the read-slice plane.

From Eq. (5), the oblique plane is defined by coordinate parameterizations

$$\begin{aligned} r_{so}(s' = 0) &= s, \\ p_{so}(s' = 0) &= p, \\ s_{so}(s' = 0) &= r. \end{aligned} \tag{6}$$

The magnet's Cartesian coordinates are then defined based on the initial ($\theta = 0°$) gradient choices. For our in vivo investigations, we used $(r, s, p) = (z, y, x)$. Eq. (6) is then used to eliminate the slice, or y coordinate, from the shim functions. Table 1 provides the resulting degenerate functions for this scenario.

A subset of linearly independent shims can be determined from this functional set. There is more than one choice and decisions can be made based on shim strengths and other system-specific restrictions. From this set, we chose $\{X, Z, Z^2, ZX, ZY, Z^3, Z^2X, Z^2Y, ZXY\}$ for our in vivo application.

To determine the shim selections for the entire range of θ, this analysis can be followed for a set of base angles $\{0, 45, 90, 135\}°$. Shim settings can be used for 45° windows centered on each base angle. Though the same analysis will hold, double-oblique settings will require an extended

Table 2
Example non-degenerate shim sets based on a single oblique angle for $(r, s, p) = (z, y, x)$ gradient orientation

Base angle (degrees)	Shim set
0	$X, Z, Z^2, ZX, X^2 - Y^2, Z^3, Z^2X, Z(X^2 - Y^2), X^3$
45	$X, Z, Z^2, ZX, ZY, Z^3, Z^2X, Z^2Y, ZXY$
90	$X, Y, Z^2, XY, X^2 - Y^2, Z^2X, Z^2Y, X^3, Y^3$
135	$X, Z, Z^2, ZX, ZY, Z^3, Z^2X, Z^2Y, ZXY$

Angular ranges are 45° centered on given base angles.

matrix providing settings for 45° windows on each angle. For the gradient choices in this study, Table 2 provides sets of non-degenerate shims for all single-oblique angle settings.

As previously mentioned, lower-order shim terms are induced when shim functions are projected into oblique planes not centered on the gradient isocenter. These interactions can be uncovered by keeping the constant of Eq. (4). Within our example, the relatively simple projected function $(z^2 - x^2)/2$ for a Z^2 shim projected on a single-oblique slice through the isocenter, becomes significantly more complicated when projected on an off center slice;

$$\frac{1}{2}(z^2 - x^2) + \sqrt{2}cz - c^2. \tag{7}$$

The off-center Z^2 projection now contains added linear and constant terms.

These interactions are internally compensated through least squares optimization. However, they can use significant strength from lower-order shims to compensate the interactions. This could become a problem as DSU is extended to higher-order shims, which will have a cascading interaction effect.

2.2. Through-slice shims

For imaging applications, typical slice widths are small enough that any through-slice inhomogeneity can accurately be truncated to the linear term. Consider the example of an axial (z sliced) imaging experiment with thin slices. The in-plane shim set will not include the XZ shim because it is degenerate in the two-dimensional X-Y plane with the X shim. In the through-slice ($\hat{z}$) direction, the XZ shim will approximate to Z and X shims. The X shim components will integrate in the through-slice direction to determine the net in-plane $\hat{x}$ component, which is then compensated by the in-plane X shim. Therefore, the through-slice inhomogeneity can accurately be compensated alone by the Z shim. This linear truncation of through-slice shims is the basis behind the success of z-shimming methods such as GESEPI [12].

As this example demonstrates, the through-slice shim in a non-oblique slicing protocol is just a linear shim in the slice direction. However, linear through-slice shims for an oblique slicing strategy must be updated in a superposition which leaves the in-plane shim field intact. We therefore must acquire a through-slice projection in the oblique-sliced direction and determine a linear trend for each slice i,

$$\Delta B_0^i = \eta_i r_s + c_i, \tag{8}$$

where r_s is the through-slice coordinate. Given a normal vector to the imaging plane

$$\hat{\mathbf{n}} = \sum_{j=1}^{3} \alpha^j \hat{\mathbf{x}}^j, \tag{9}$$

where the $\hat{\mathbf{x}}^j$ represent Cartesian unit vectors. We can then add through-slice compensation for each linear shim within slice i according to

$$x_i^j = \eta_i \alpha^j, \tag{10}$$

without altering the in-plane shim setting. In this expression, x^j represents the adjustment in current setting for shim j (e.g., x^1 represents the change in the X shim.)

For our in vivo application, the normal to the oblique plane was given by

$$\hat{\mathbf{n}} = \cos\theta\hat{\mathbf{y}} - \sin\theta\hat{\mathbf{z}}.$$

After determining the coefficients η_i with slice projections, the Y and Z shim settings were then updated according to

$$x_i^2 = \eta_i \cos\theta \ (Y \text{ shim}),$$
$$x_i^3 = -\eta_i \sin\theta \ (Z \text{ shim}).$$

3. Materials and methods

3.1. Basic NMR acquisition parameters

DSU was implemented in the W.M. Keck High Field Magnetic Resonance Laboratory on a 4.0 T Magnex (Oxford, UK) magnet (bore diameter = 94 cm) interfaced to a Bruker (Ettlingen, Germany) Avance spectrometer. Actively shielded linear gradients and a Z_0 coil were housed in a Bruker head-gradient insert which can switch 30 mT/m in 150 μs (gradient diameter = 38 cm). A Magnex whole-body gradient system housed the second and third-order shim assemblies (shim diameter = 72 cm). RF reception and transmission were carried out by a Bruker TEM coil (inner diameter = 26 cm).

3.2. Dynamic shimming interface

DSU relies upon the ability to rapidly change electronic settings in shim amplifiers. To minimize electronic updating time, optimal shim settings were stored in local hardware memory. From there they were converted to analog voltages and sent to pre-emphasis and Z_0 compensation circuits and finally on to the input of the shim amplifiers (Model MXH-14 ± 10 A with ±95 V voltage rails, Resonance Research, Billerica, MA). To establish and control this data flow, a custom-built Dynamic shimming interface (DSI) was placed in communication with the shim amplifi-

ers, Bruker spectrometer control computer, and a dedicated processing computer.

Software written in Microsoft Visual Basic (Microsoft, Seattle, WA) allowed for uploading of optimal shim settings from the processing computer to the DSI hardware memory via RS232 connection. The DSI could store a global setting and up to 127 slice-specific settings for all zeroth through third-order shims. The DSI was also networked via RS232 to the Bruker control computer running ParaVision 3.0 for routine shimming. NMR Control words within the pulse program were used to accurately initiate changes for all first through third-order shims . This hardware configuration could electronically implement shim changes on a 100 μs time scale. However, to minimize transient gradient amplitude oscillations, short time-constant eddy currents (see below), and significantly reduce acoustic noise, a 500 μs/A ramp was imposed on all shim changes, resulting in a 5 ms ramp for a 100% shim change.

3.3. Eddy current compensation

Rapid shim changes induce transient eddy currents in a magnet's cooled conducting structures. Gradient pre-emphasis [13] was implemented on the shim changes to reduce these effects. An analog pre-emphasis system with digital control over amplitudes and time constants was developed and interfaced to a processing computer for user input and control.

B_0 and identical multipole eddy-fields for changes in all zeroth through second-order shims were measured on a long water-filled tube placed in a direction uniquely defining a component of the shim under investigation. The tube was narrow (2 cm) relative to length (20 cm) to minimize the effects of cross-term eddy-currents. Measurements were timed beginning immediately after the ramp-down of the shim changes. The B_0, linear, and second-order eddy-effects were estimated from the spatially dependent phase difference between 26 readout profiles along the tube in the absence and presence of 25% shim changes. The shielded Z_0 and first-order shims did not produce appreciable eddy-fields. The unshielded second-order shims all yielded significant eddy-effects requiring B_0 compensation and pre-emphasis of the same order. Linear eddy currents were negligible for all second-order shims. Table 3 provides a summary of the eddy-current characterization exponentials. Some second-order pre-emphasis pulses were found to induce additional B_0 eddy currents. It was therefore imperative to set pre-emphasis exponentials first, thus allowing the B_0 compensation to remove eddy-fields from both the pre-emphasis and pure shim changes.

Table 3
B_0 compensation and shim pre-emphasis exponential characteristics for second-order shims

Shim (strength Hz/cm^2/%)	B_0 TC (ms)	B_0 Amp (Hz/%)	Pre-emph TC (ms)	Pre-emph Amp (Hz/cm^2/%)
Z^2 (0.18)	118.4	17.9	175.0	0.02
	21.4	11.6	78.8	0.09
	6.95	−20.1	2.0	0.03
$X^2 - Y^2$ (0.13)	NS	NS	107.0	0.03
	NS	NS	3.9	0.02
XY (0.25)	60.0	0.1	91.2	0.05
	NS	NS	2.3	0.04
ZX (0.48)	50.0	0.3	745.0	0.03
	NS	NS	83.6	0.10
	NS	NS	1.6	0.09
ZY (0.47)	95.6	−0.1	373.0	0.02
	5.4	−1.0	85.0	0.09
	NS	NS	1.7	0.07

Amplitudes are given for 1% changes in the shim.
NS, not significant; TC, time constant; Amp, amplitude.

Fig. 2 displays eddy-field reduction using B_0 compensation and pre-emphasis on Z^2 shim changes.

3.4. Shim determination protocol

Magnetic-field maps were calculated from a series of asymmetric gradient-echo phase-maps with increased asymmetrizing delays. Complex phases were calculated relative to the first delay and by using a short initial delay of 0.5 ms, it could be assumed that the phase difference between the first and second delay was unwrapped. The remaining phases were then temporally unwrapped by extrapolating upon the linear trend established by the first two temporal points. Finally, ΔB_0 was determined through a linear least-squares fit of the unwrapped phase vs. delay trend. Increased accuracy and sensitivity of B_0 maps can be attained by increasing the number of delay point acquisitions and extending the evolution delays.

In-plane least squares optimization over the spherical harmonic shim functions was performed using software developed in C calling MINPACK's [14] Levenberg-Marquardt routine. Optimization ROIs were selected using a Matlab (Mathworks, Natick, MA) GUI to specify a subset of elliptical ROIs throughout the slice distribution. The full ROI set for the slice distribution was then interpolated using these scout ellipses. This method allowed for efficient real-time in vivo ROI determination for experiments with large numbers of slices. For fewer slices, manual polygon selection of each slice-specific ROI is possible. Through-slice linear projections were acquired using a 1D analogue of the in-plane mapping sequence. The readout was directed in the through-slice direction and slice-selective projections were acquired while updating the in-plane optimal shim settings. Matlab code extracted the residual through-slice B_0 maps from this data and determined the linear best-fit for each slice. The total in-plane and through-slice shim determination time, including acquisition, processing, and optimization, for a $64 \times 64 \times 32$ acquisition matrix was approximately 5 min.

3.5. Acquisition parameters

In vivo B_0 maps were acquired with (a) no updating, (b) updating first-order shims, and (c) updating first and second-order in-plane shims. The static global shim was

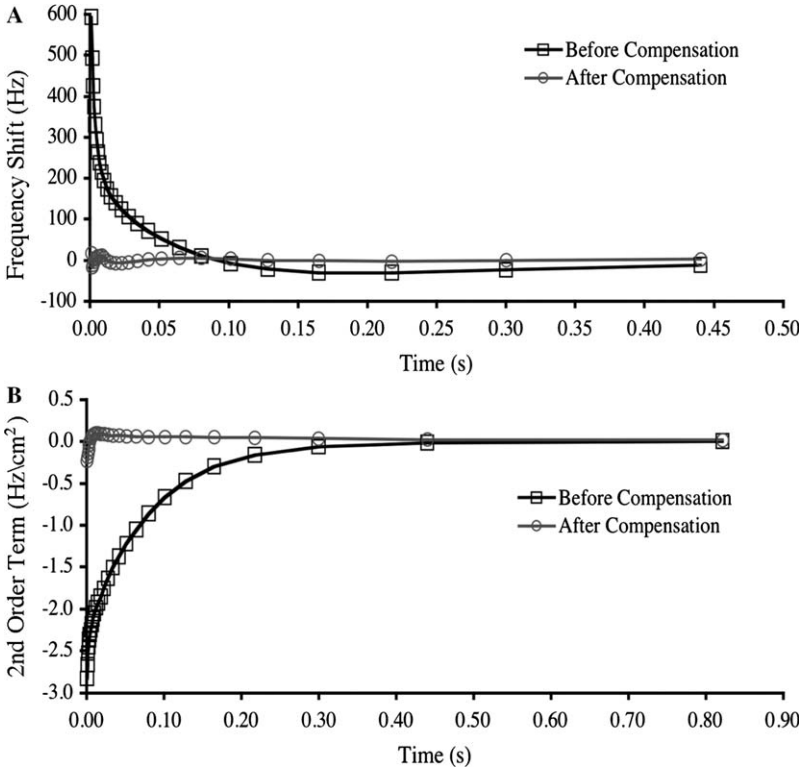

Fig. 2. (A) B_0 and (B) Z^2 pre-emphasis eddy current compensation for 25% Z^2 shim change.

determined using a Bruker-supplied second-order FASTMAP [15] protocol with a cubic ROI of side length 6.5 cm centered on the posterior part of the corpus callosum. Elliptical DSU ROIs were chosen to maximize brain inclusion in each slice.

Improvement using DSU was diagnosed for both single-oblique and non-oblique slicing geometries.

Field maps were acquired for non-oblique axial slicing while dynamically updating zeroth through second-order shims as outlined in Table 2 for the $\theta = 90°$ case. For the single-oblique scenario, axial-coronal (YZ)-sliced maps were acquired with an angle of $\theta = 65°$ with respect to the Z axis. Zeroth through second-order shims as listed in the $\theta = 45°$ category of Table 2 were updated.

For each map, 32 adjacent 4 mm slices were distributed through the brain with 96×96 in-plane pixels over 25.6×25.6 cm in-plane resolution. Four echo delays of 0, 0.5, 1.5, and 4.0 ms were used with total pulse repetition time $TR = 800$ ms, (or inter-slice $TR = 25$ ms), and zero-delay echo-time $TE = 4$ ms. Multiple datasets were acquired to establish intra-subject variation. For each slicing strategy, data were acquired from $N = 3$ independent subjects.

Using these field maps, slice-specific frequency-offset histograms on the DSU optimization ROI were calculated using 1 Hz bin widths. These distributions did not adhere to any simple statistical models. Therefore, widths were determined using the central range containing 80% of the total pixels. This is a generalization of an interquartile range calculation, which uses a 50% criterion [16].

An important issue in the development of DSU is the inclusion of third-order shims. Experimentally it was found that all seven third-order shims induced significant eddy-currents with third-order (e.g., $Z^3 \to Z^3$), zeroth-order (e.g., $Z^3 \to B_0$), and in many cases first-order (e.g., $Z^3 \to Z$) multipole components. Eddy-current compensation of third-order shims would have required more than fifty additional time constants, making the pre-emphasis circuitry unwieldy and impractical. Furthermore, the pre-emphasis amplitudes would seriously limit the (already weak) third-order shim amplitudes. To investigate the benefit of including third-order shims, a simulated third-order DSU data set was constructed using the static globally-shimmed B_0 map. Slice-specific third-order shims (in addition to the zeroth through second-order shims) were then computationally removed as prescribed in the previous degeneracy analysis.

To ascertain DSU effectiveness over different oblique-slicing geometries, single oblique ($\phi = 0$) slicing geometries for values of θ ranging from 0 to 175° in 5° increments were simulated from the axial ($\theta = 90°$) field maps previously described. Optimal settings for angle-specific non-degenerate shim sets were calculated using simulated maps over manually traced ROIs encompassing the entire brain. The resultant inhomogeneity was then determined by subtracting the optimum shim fields from the simulated maps on a slice-specific basis. Using these resultant field maps, global homogeneity was determined from the 80% of histograms using all pixels within the whole-brain ROI. This process was repeated including (a) up to 1st order, (b) up to 2nd

order, and (c) up to 3rd order shims in the simulated DSU optimization.

Single-shot gradient-echo EPI images were acquired over ten 4 mm thick slices with 64×64 in-plane pixels over 25.6×25.6 cm, $TE = 25$ ms, $TR = 2500$ ms, and effective phase encoding bandwidth 1 kHz (16 Hz/pixel). Images were collected under both static global and DSU shim settings. Each shim setting was determined using the previously described methods. For geometric reference, a spin-echo image of the same geometric character was acquired using $TE = 10$ ms and $TR = 2000$ ms.

4. Results

4.1. B_0 map imaging

Fig. 3 illustrates significant DSU-utilized homogeneity improvement in axial slices local to the frontal sinuses. Following static global shimming with up to second-order shims, the global map illustrates the severe residual inhomogeneity encountered in the frontal cortex of the brain. Field inhomogeneity of up to 150 Hz can readily be encountered a few centimeters into the brain. The field map acquired using DSU demonstrates significantly reduced frontal lobe inhomogeneity.

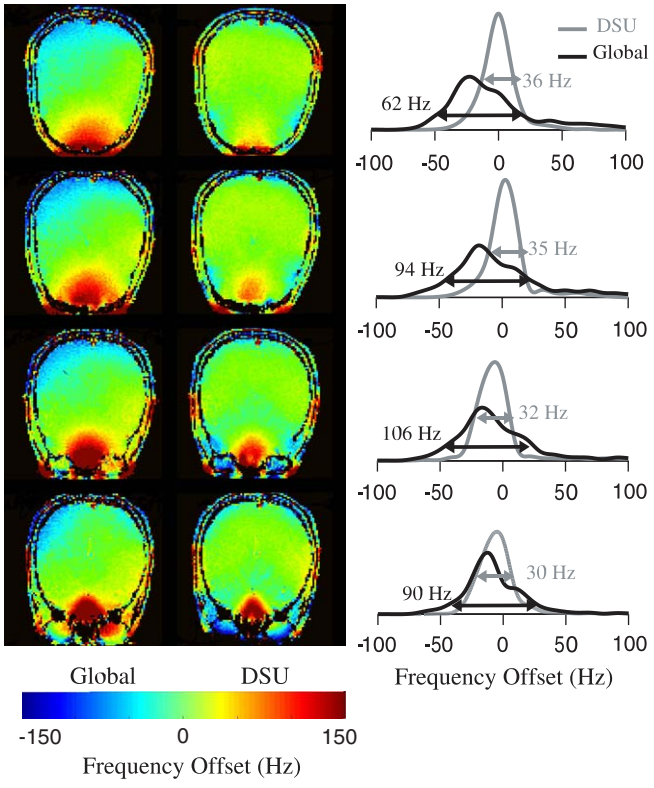

Fig. 3. Non-oblique-sliced DSU homogeneity improvement for selected slices in a 32-slice acquisition. For each slice, B_0 maps are shown using a static global FASTMAP optimized shim and second-order DSU. Frequency offset histograms collected over the entire brain are shown for each shim setting in each slice. 80% widths of each distribution are labeled.

Fig. 4 displays homogeneity improvement across slices and orders of shims included in the optimization for (A) non-oblique axial-sliced DSU and (B) single-oblique axial-coronal-sliced DSU. The global inhomogeneity distribution varied widely across subjects. However, as more shims are included in the optimization, distribution shapes converge. All subjects followed the trends illustrated in Fig. 3. For both slicing orientations, the homogeneity converged and was optimal within the limitations of lower-order shims.

Homogeneity improvement with increasing shim inclusions can be quantified by averaging the improvement in slice-specific magnetic-field offset distribution widths when compared to the static global shim setting. Averages were calculated across all subjects for each order of shim included. Though the width distributions are not perfectly Gaussian, a standard deviation of the improvements does provide a rough approximation for the range of homogeneity improvement. For non-oblique axial slicing, successive average improvements are given by 12.7 ± 12.5, 7.8 ± 6.9, and 3.3 ± 3.1 Hz for inclusion of first, then second, and finally third-order shims in the dynamic optimization. For single-oblique axial-coronal slicing, improvements for first, second, and third-order inclusions were given by 14.6 ± 12.3, 11.1 ± 8.1, and 4.3 ± 4.1 Hz. These results should not be used to quantitatively compare axial and oblique slicing geometries. Such a comparison requires optimization and analysis over whole-brain ROIs for a wide range of slice angulations, which is presented in the next section. Rather, these results present the DSU-utilized shim inclusion dependence when optimizing over rapidly constructed, maximal brain inclusion, slice specific, elliptical ROIs. The results show a clear advantage in using both first and second-order shims in DSU. The improvement between second and third-order DSU on the human brain is not as obvious. While there are a few isolated slices that do benefit from the simulated third-order DSU, the majority of slices in both slicing geometries improve by only a few hertz. This is because the majority of inhomogeneity within the slices are either first, second, or far higher in spherical harmonic order. This leaves third-order shims limited in value for whole-slice optimized dynamic shimming on the human brain.

4.2. Single oblique slicing survey

As reported by Tyszka and Mamelak [17], B_0 inhomogeneity varies significantly with head pitch relative to the static field. It is thus imperative to analyze DSU-utilized global homogeneity within narrow head pitch ranges. Hence, an anatomic reference was used to register head pitch across subjects. Fig. 5 presents the simulated survey of global homogeneity for one single-oblique strategy (axial-coronal). The oblique angle is measured relative to the coronal plane and data are presented for two subjects with head pitch within 2° of one other. As expected, increasing shim inclusions reduce the variation

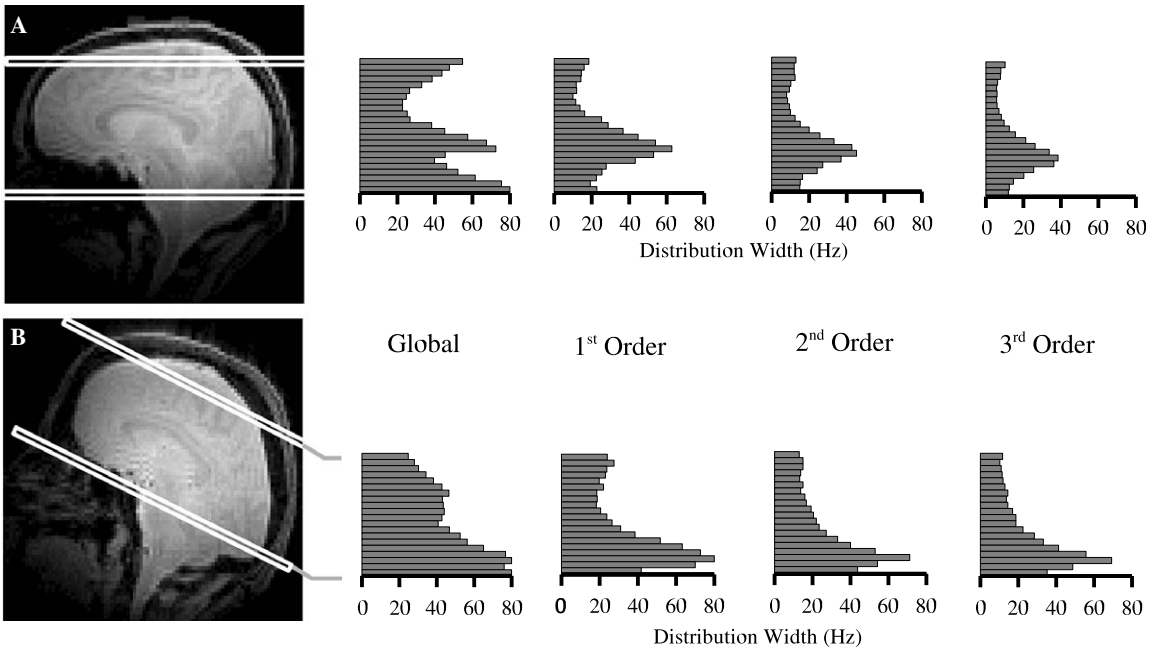

Fig. 4. DSU improvement across included shim orders quantified using histograms of residual-field homogeneity within optimization ROIs. Global, first, and second-order data are experimental results, while third-order results are simulated from the global experimental data. Results are presented for (A) non-oblique axial slicing and (B) single-oblique axial-coronal (YZ, $\theta = 65°$) slicing. Histogram widths, as visualized in Fig. 2, are calculated using an 80% criterion.

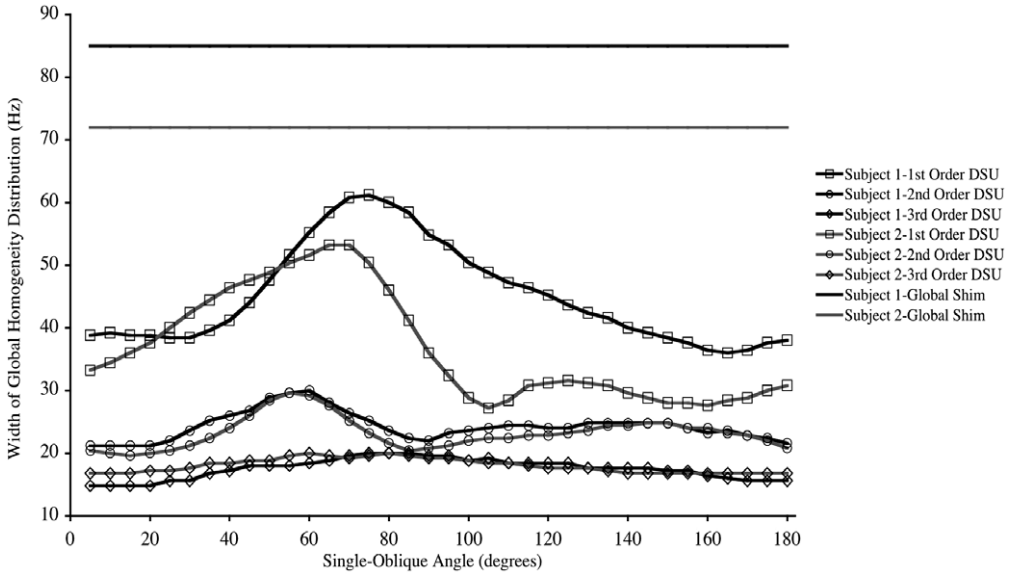

Fig. 5. DSU-utilized global homogeneity survey across shim inclusions and single-oblique angle for two subjects of similar head pitch. Homogeneity is quantified by the width of frequency offset histograms sampled over the entire brain.

of subject-specific homogeneity-slicing-angle trends. Notice that a slight maximum in global inhomogeneity using second-order shims occurs at approximately $\theta = 65°$, which agrees with the truncated ROI, slice-specific analysis of Fig. 4, where the oblique diagnostic at $\theta = 65°$ demonstrated slightly more residual inhomogeneity than that of the axial-sliced ($\theta = 90°$) diagnostic. Significant global homogeneity for all slicing angles is gained in moving from static to first-order DSU and similarly with the inclusion of second-order shims. However, it is clear that improvement with the inclusion of third-order shims is significantly reduced across all slicing angles, with a maximum improvement of 8 Hz at the 60° slicing angle. Whole-brain global homogeneity improvement of 8 Hz will not likely have significant implications for any imaging applications. Similarly, while global homogeneity

has a clear oblique angular dependence for first-order DSU, the angular dependence for up to second-order DSU, shows significantly reduced variation. This dependence is similarly reduced for up to third-order DSU.

4.3. Echo-planar imaging

Echo planar imaging is more susceptible to inhomogeneity-induced geometric distortion and signal loss than standard gradient-echo imaging due to longer T_2^* influenced phase evolution between phase-encoding blips. Homogeneity improvement can thus be diagnosed through signal recovery and reduced geometric distortion (improved in-plane homogeneity).

Fig. 6 demonstrates improvement in geometric distortion comparing EPI images with a static global shim and second-order DSU. Improvement in the EPI images depends on slice position. The upper slice (left) shows limited improvement due to its initial lack of significant inhomogeneity. The middle slice shows signal recovery in the frontal cortex and reduced image distortion in the posterior part of the brain (white arrow). The lower slice is in the proximity of the auditory and sinus cavities, and has some of the most severe inhomogeneity in the brain. Even with DSU, zeroth through third-order shims cannot perfectly compensate this in-plane inhomogeneity. Significant signal voids are also noticeable due to residual through-slice inhomogeneity. This observation is validated quantitatively in Fig. 3 where histogram bin widths over the field homogeneity improve very little in these slices. However, DSU is able to reduce the inhomogeneity to such an extent that the resulting EPI is recognizable, has minimal geometric distortion, minimal signal loss, and is in reasonable agreement with the spin-echo MRI (dotted lines).

5. Discussion

The feasibility and utility of dynamic shim updating for human imaging studies has been presented. We have demonstrated significant global homogeneity improvement through dynamic local updating of shim settings. A method of shimming oblique slices through generalized two-dimensional degeneracy theory has been outlined and experimentally verified. MRI-based field maps have provided quantitative homogeneity assessment and in vivo EPI experiments have demonstrated the dramatic impact of DSU on fast gradient-echo imaging strategies.

fMRI relies upon gradient-echo EPI to map neural activation through measurement of the blood oxygen level dependent (BOLD) signal. T_2^* induced dephasing during extended k-space sampling results in unreliable activation localization and compromised BOLD SNR. With static shimming, the anterior frontal and temporal regions of the human brain possess inhomogeneity which renders local BOLD measurements unreliable. Diffusion tensor imaging (DTI) and tractography also rely on dynamic gradient-echo imaging techniques. The accuracy of diffusion tract mapping deteriorates in the presence of field inhomogeneity [18]. Hence, both of these growing fields can benefit greatly from DSU implementation.

Inhomogeneity effects can be reduced in EPI through increasing the number of interleaves, thereby reducing k-space sampling. However, this also increases the repetition time (TR) and most dynamic EPI studies have time resolution requirements which limit TR extension. Therefore, many protocols are forced to use single-shot (one interleave) EPI. Furthermore, interleaved EPI can lead to significant ghosting artifacts.

Several approaches have recently been developed to reduce image artifacts in single-shot EPI. By collecting

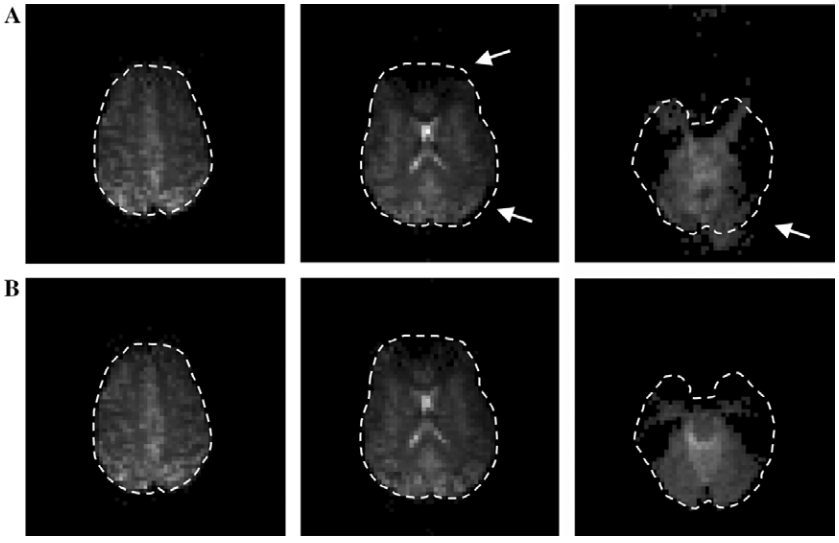

Fig. 6. EPI images (A) without and (B) with second-order DSU for axial slices (from left to right) 2 cm below the top of the skull, 1 cm above the nasal cavity, and through the hippocampal region. The white dotted lines indicate the brain contours as extracted from a high-bandwidth spin-echo MRI. White arrows designate areas of significant image quality improvement.

MRI-based field maps, geometric distortion can be corrected through post-acquisition processing [19]. However, this method is incapable of recovering through-slice signal loss. At the expense of lower SNR, distortion can also be reduced through parallel imaging using the sensitivity encoding (SENSE) protocol [20], whereby k-space sampling time is reduced. Phase refocusing [21] through modulated RF pulses can reduce through-slice signal loss, at the expense of higher pulse peak power and the complication of real-time complex RF pulse design. Furthermore, with increasing B_1 inhomogeneity at high magnetic fields this option induces its own problems. Through modulation of slice selection gradients, methods such as gradient-echo slice excitation profile imaging (GESEPI) [12] can also reduce through-slice signal loss. Used in combination, SENSE and GESEPI have demonstrated significant reduction of image artifacts [22] in single-shot EPI. GESEPI, however, requires multiple acquisitions for each slice. To retain sufficient time resolution, this requires multiple-echo sequencing, which is acceptable and feasible for imaging, but not for spectroscopic imaging (SI), where J coupling will induce unwanted coherences throughout the echo-train, and long acquisition times (e.g., 100 ms) will lead to unacceptable T_2 losses.

A number of alternative hardware methodologies have also been presented in recent years to deal with previously unshimmable inhomogeneity within the human brain. A universal ferromagnetic passive shim array [3] optimized over population-averaged field maps has been shown to reduce global inhomogeneity. However, such an approach does not account for inter-subject variations. Our investigations have shown such variations to be very significant. Shims placed in the patient's mouth have also been presented in both the passive [4] and active [5] regime. Both have been shown to reduce inhomogeneity local to the frontal lobe, and each has the capability to adjust to subject variations. However, these devices introduce significant patient discomfort and are limited by their extremely localized effects. Since they are developed on a trial and error basis, further development of their homogenizing capability is a difficult task.

Dynamic shim updating is a general approach to achieve global homogeneity during multi-slice acquisition. As such, DSU can be used with a wide variety of sequences, coils and applications while still providing subject-specific homogenizing capacity. However, DSU has its own specific challenges and limitations.

Eddy currents stand out as the most noticeable challenge in the deployment of DSU technology. Among the first and second-order shims, Z^2 demonstrated the most extreme eddy currents. It induced eddy-fields with amplitudes of (17.9, 11.6, -20.1) Hz and time constants of (118.4, 21.4, 6.95) ms for the B_0 channel and amplitudes of (0.02, 0.09, 0.03) $\frac{\text{Hz}}{\text{cm}^2}$ with time constants of (175.0, 78.8, 2.0) ms for the pre-emphasis channel. Due to their orientation with respect to the cryostat, zonal shims will always induce the most significant eddy-currents. Higher-order zonal shims will generate even more severe eddy-fields, with cascading interactions among lower-order zonal fields.

With our unshielded shim set, pre-emphasis occupies a significant fraction of the total available shim-strength. The pre-emphasis channel for the Z^2 shim reduces its available strength by 75%. The remaining shim strength is able to adequately compensate all but the most severe inhomogeneity. However, this problem will become untenable with higher-order zonal shims. At the expense of lengthened repetition times, one can extend the ramp-time for shim changes and remove the need to compensate the shortest eddy currents. This is an option for spectroscopic applications but not always for EPI utilization of DSU.

Actively-shielded shims are crucial in mediating the pre-emphasis issue. Developments have been made in the design of actively shielded shims [23] and low-order zonal shielded shims are widely available. As with shielded imaging gradients, shielded shims still require pre-emphasis. Even with the reduced amplitude of shielded shims, it is likely that the remaining shim strength after pre-emphasis will be far greater than that of the unshielded variety. Thus, the extension of DSU to higher-order shims would rely heavily upon the availability and use of actively shielded shims.

The experimental and analytic results presented here demonstrate that DSU may be applied to arbitrary oblique slices with a substantial improvement in whole brain homogeneity over static shim settings. The inclusion of second and third-order shims in DSU significantly reduces the dependence of global homogeneity on oblique slicing angle. In all cases, greater fractional improvement may occur in individual slices, or specific regions within individual slices, than over the entire brain. Furthermore, the exact manifestation of image artifacts will depend on the orientation of the phase-encoding direction relative to the remaining magnetic-field inhomogeneity. A full interpretation of these effects will require specific impact investigations of shim inclusion and slicing-angle on signal loss and pixel shifts.

When modeling inhomogeneity in a global fashion, there are significant third-order effects that can be compensated. However, our results show that third-order inhomogeneity becomes more limited in scope when modeling in two dimensions over entire slices. We have observed a subject-averaged whole-slice homogeneity improvement of approximately 3–4 Hz when dynamically updating third-order shims. While a few isolated slices may see more pronounced artifact reduction, improvements across the entire volume of only a few hertz will not be significant for EPI. When one is not interested in whole-slice homogeneity, the inclusion of third-order shims has been shown to significantly improve homogenization within localized regions (e.g., the hippocampus) of the human brain [25]. In addition, simulations of slice-specific third-order shimming on the mouse brain at 9.4 T have shown significant improvements in residual inhomogeneity. Although the optimal

currents required in these simulations were well outside of currently available shim strengths, these results indicate that spectroscopic imaging of mice and rat brains could benefit from dynamic updating of third-order shims [26].

The choice of slice-specific optimization ROIs could be construed to effect the global homogenization capabilities of DSU. To address this issue, DSU was implemented using both elliptical and manually-traced ROIs maximally encompassing the entire brain. When compared to optimization over elliptical ROIs, the use of manually-traced ROIs demonstrated limited global homogeneity improvement. This is due to the fact that areas added in the manual trace typically have higher-order inhomogeneity, which does not weigh heavily into the low-order optimization over the entire slice.

In spite of the aforementioned technical challenges, second-order DSU is feasible on the human brain and stands as the most effective and viable manner to maximize global homogeneity within the limitations of spherical harmonic shim technology.

This paper has highlighted DSU's virtues within the imaging community. However, application of DSU to spectroscopic studies is also significant. Rapid DSU will allow spectroscopic information from vastly different regions of the brain to be acquired within a single TR. Future work will demonstrate the application of DSU to multi-volume spectroscopy and spectroscopic imaging.

Acknowledgments

The authors thank Mark Abildgaard for assistance in construction of electronic equipment. We also acknowledge Bruker support (Roy Gordon and Hans Post) for assistance concerning shim pre-emphasis and Piotr Starewicz for valuable discussion on a variety of topics. Grant sponsors: NIH; Grant Nos: BRP R01 EB000473 and R21 CA118503 (to R.A.G.), Pfizer Inc., W.M. Keck Foundation.

References

[1] J.D. Jackson, Classical Electromagnetism, John Wiley and Sons, New York, 1999.
[2] D.I. Hoult, R. Deslauriers, Accurate shim coil design and magnet-field profiling by a power minimization matrix method, J. Magn. Reson. 108A (1994) 9–20.
[3] A. Jesmanowicz, J.S. Hyde, W.F.B. Punchard, P.M. Starewicz, Method for shimming a magnetic field in a local MRI coil, US Patent 6,294,972, 2001.
[4] J.L. Wilson, M. Jenkinson, P. Jezzard, Optimization of static field homogeneity in human brain using diamagnetic passive shims, Magn. Reson. Med. 48 (2002) 906–914.
[5] J.J. Hsu, G.H. Glover, Mitigation of susceptibility-induced signal loss in neuroimaging using localized shim coils, Magn. Reson. Med. 53 (2005) 243–248.
[6] A.M. Blamire, D.L. Rothman, T.W. Nixon, Dynamic shim updating: A new approach towards optimized whole brain shimming, Magn. Reson. Med. 36 (1996) 159–165.
[7] R.A. de Graaf, P.B. Brown, S. McIntyre, D.L. Rothman, T.W. Nixon, Dynamic shim updating (DSU) for multislice signal acquisition, Magn. Reson. Med. 49 (2003) 409–416.
[8] G. Morrell, D. Spielman, Dynamic shim updating (DSU) for multislice magnetic resonance imaging, Magn. Reson. Med. 38 (1997) 477–483.
[9] J. Shen, Effect of degenerate spherical harmonics and a method for automatic shimming of oblique slices, NMR Biomed. 14 (2001) 177–183.
[10] D.H. Kim, E. Adalsteinsson, G.H. Glover, D.M. Spielman, Regularized higher-order in vivo shimming, Magn. Reson. Med. 48 (2002) 715–722.
[11] H. Goldstein, Classical Mechanics, Addison-Wesley, Reading, MA, 1980.
[12] Q.X. Yang, G. Williams, R. Demeure, T. Mosher, M.B. Smith, Removal of local field gradient artifacts in T_2^*-weighted images at high fields by gradient-echo slice excitation profile imaging, Magn. Reson. Med. 39 (1998) 402–409.
[13] J.J. van Vaals, A.H. Bergman, Optimization of eddy-current compensation, J. Magn. Reson. 90 (1990) 52–70.
[14] J.J. More, D. Sorensen, K.G. Hillstrom, B.S. Garbow, Argonne National Laboratory Reports, User Guide of MINPACK-1, ANL-80-74, 1980.
[15] R. Gruetter, Automatic, localized in vivo adjustment of all first- and second-order shim coils, Magn. Reson. Med. 29 (1993) 804–811.
[16] D.J. Sheskin, Handbook of Parametric and Nonparametric Statistical Procedures, CRC Press, Boca Raton, FL, 2000.
[17] J.M. Tyszka, A.N. Mamelak, Quantification of B_0 homogeneity variation with head pitch by registered three-dimensional field mapping, J. Magn. Reson 159 (2002) 213–218.
[18] J.L. Andersson, M. Richter, W. Richter, S. Skare, R.G. Nunes, M.D. Robson, T.E. Behrens, Effects of susceptibility distortions on tractography, Proc. ISMRM 11 (2004) 87.
[19] P. Jezzard, R.S. Balaban, Correction for geometric distortion in echo planar images from B_0 field variations, Magn. Reson. Med. 34 (1995) 65–73.
[20] K.P. Pruessmann, M. Weiger, M.B. Scheidegger, P. Boesiger, SENSE: sensitivity encoding for fast MRI, Magn. Reson. Med. 42 (1999) 952–962.
[21] N. Chen, A.M. Wyrwicz, Removal of intravoxel dephasing artifact in gradient-echo images using a field-map based RF refocussing technique, Magn. Reson. Med. 42 (1999) 807–812.
[22] Q.X. Yang, J.W. Wang, M.B. Smith, M. Meadowcroft, X. Sun, P.J. Eslinger, X. Golay, Reduction of magnetic field inhomogeneity artifacts in echo planar imaging with SENSE and GESEPI at high field, Magn. Reson. Med. 52 (2004) 1418–1423.
[23] L.K. Forbes, S. Crozier, A novel target-field method for magnetic resonance shim coils: shielded zonal and tesseral coils, J. Phys. D: Appl. Phys. 36 (2003) 68–80.
[25] H.P. Hetherington, J.W. Pan, An automated shim mapping method for spectroscopic imaging of the human hippocampus, in: Proceedings of the 13th ISMRM, 2005.
[26] N. Miyasaka, K. Takahashi, H.P. Hetherington, Fully automated shim mapping method for spectroscopic imaging of the mouse brain at 9.4 T, Magn. Reson. Med. 55 (2006) 198–202.